Nanoparticle O–H Bond Dissociation Free Energies from Equilibrium Measurements of Cerium Oxide Colloids

Rishi G. Agarwal, Hyun-Jo Kim, and James M. Mayer*

Department of Chemistry, Yale University, New Haven, CT 06520-8107, USA
*Corresponding author, james.mayer@yale.edu

Abstract. A novel equilibrium strategy for measuring the hydrogen atom affinity of colloidal metal oxide nanoparticles is presented. Reactions between oleate-capped cerium oxide nanoparticle colloids (nanoceria) and organic proton-coupled electron transfer (PCET) reagents are used as a model system. Nanoceria redox changes, or hydrogen loadings, and overall reaction stoichiometries were followed by both ^{1}H NMR and X-ray absorption near edge spectroscopies. These investigations revealed that, in many cases, reactions between nanoceria and PCET reagents reach equilibrium states with good mass balance. Each equilibrium state is a direct measure of the bond strength, or bond dissociation free energy (BDFE), between nanoceria and hydrogen. Further studies, including those with larger nanoceria, indicated that the relevant bond is a surface O–H. Thus, we have measured surface O–H BDFEs for nanoceria – the first experimental BDFEs for any nanoscale metal oxide. Remarkably, the measured CeO–H BDFEs span 13 kcal mol^{-1} (0.56 eV) with changes in the average redox state of the nanoceria colloid. Possible chemical models for this strong dependence are discussed. We propose that the tunability of ceria BDFEs may be important in explaining its effectiveness in catalysis. More generally, metal oxide BDFEs have been used as predictors of catalyst efficacy that, traditionally, have only been accessible by computational methods. These results provide important experimental benchmarks for metal oxide BDFEs and demonstrate that the concepts of molecular bond strength thermochemistry can be applied to nanoscale materials.

Introduction

Redox-active metal oxide materials and nanomaterials are important technologically and in the environment.[1–6] Many of the redox transformations they perform involve the transfer of hydrogen atoms (protons and electrons).[7–11] As a result, free energies of hydrogen atom transfer to and from these materials are fundamental thermochemical values of great importance. This report's emphasis on nanoparticle bond strength thermochemistry follows the longstanding interest in surface–H and surface–X adsorption energies in surface science,[12,13] and the use of such energies as descriptors in the popular 'scaling relationship' and 'volcano plot' analyses of heterogeneous catalysis and electrocatalysis.[14–17] Despite wide interest, measurements of surface–H adsorption energies have almost entirely been restricted to single crystal metals and ultrahigh-vacuum conditions.[12,18] Computed adsorption energies are more widely reported. However, especially for binary materials such as redox-active oxides, they often rely on assumptions about the stoichiometry and structure of the material's surface and little data exists for their validation.[12,19,20] As a result, there is a need for more methods to measure adsorption energies for chemically reactive materials under solution conditions. Here we report the first free energy measurements of the bond strength between hydrogen and a metal oxide nanomaterial, and explore how those bond strengths change with the hydrogen stoichiometry of the oxide. This advance is enabled by a novel equilibrium method which is applied to reactions between cerium oxide nanoparticle colloids and molecular reagents (Scheme 1).

Scheme 1. Equilibrium between cerium oxide nanoparticles and a substituted 1,4-hydroquinone.

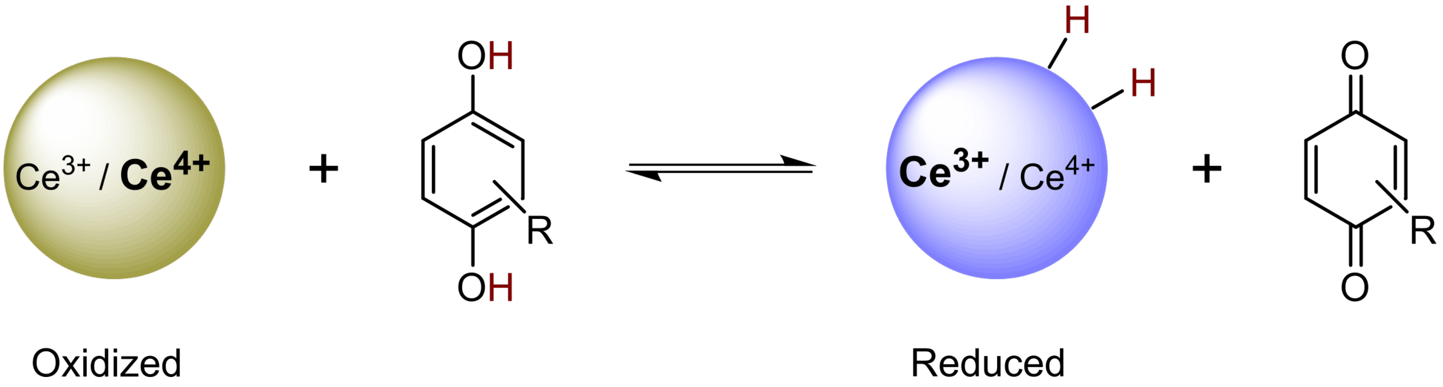

Cerium oxide (ceria) is a prototypical mixed-valence oxide, typically containing both Ce^{4+} and Ce^{3+} ions, which can vary its stoichiometry and average redox state (%Ce^{3+}) in redox reactions. This phenomenon has been the subject of significant study, and is especially pronounced at the nanoscale (nanoceria).[21–28] In nanoceria, the extent to which the %Ce^{3+} can be varied is enhanced by greater surface-to-bulk ratios, which stabilize Ce^{3+} sites. This wide range of accessible redox states is important to ceria's applications as a catalyst, co-catalyst, and reducible oxide support. In modern 'three-way' automotive catalytic converters, for example, ceria acts as a source and sink for redox equivalents to facilitate both the reduction of nitric oxide and the oxidation of carbon monoxide.[23] Ceria also catalyzes the methanation of CO_2, the hydrogenation of various alkynes, and other reactions.[19,29–34] Furthermore, aqueous suspensions of nanoceria are being explored to treat ailments caused by reactive oxygen species.[24,25,35–37] All of these applications depend on variations in the %Ce^{3+} of the ceria.

Redox reactions of ceria typically occur by the transfer of either hydrogen or oxygen atoms, and therefore the thermochemistry of these atom-transfer reactions is central to understanding ceria's reactivity. Under high-temperature conditions, the Ce^{3+}/Ce^{4+} mixed valency is most commonly balanced by oxygen vacancies in the fluorite lattice, and the material is written as CeO_{2-x}.[38] The thermochemistry of oxygen loss at bulk ceria is known to be modulated by the material's average redox state.[26,27,39,40] At closer to ambient temperatures, or in colloidal suspensions, charge balance can instead be maintained by hydrogen atom binding (because loss of H_2O is less favorable, see below).[26,33] As with many reducible metal oxides,[10,41,42] hydrogen atom addition ($H^\bullet \equiv e^- + H^+$) to ceria is most commonly thought to result in the reduction of one Ce^{4+} to Ce^{3+}, with protonation of one oxide to hydroxide ($CeO_x(OH)_y$).[43] The thermochemistry for binding hydrogen to materials is typically described as the hydrogen adsorption energy. This is the free energy or enthalpy of dissociative H_2 chemisorption to form surface–H. For ceria these values have only been accessible by computation, and reported $CeO_2(111)$ surface O–H bond strengths vary significantly between studies.[29,44,45] These papers, like most that compute H adsorption on binary materials, report single values for the hydrogen adsorption energy. However, a recent computational study of Ce_nO_{2n} nanoclusters described significant heterogeneity in the hydrogen adsorption energy between different surface sites.[46] Experimental measurements of the low-temperature thermochemistry of ceria–and other metal oxides–are needed as benchmarks and to clarify whether the single bond strength model is appropriate for these complex surfaces.

The preferred thermochemical descriptor for hydrogen binding in *solution* reactions is the standard free energy of bond homolysis, called the bond dissociation free energy (BDFE), eq 1.[47,48]

$$\text{X–H} \rightarrow \text{X}^\bullet + \text{H}^\bullet \qquad \Delta G^\circ = \text{bond dissociation free energy, BDFE} \tag{1}$$

We use BDFEs in this paper because they have been reported for a wide variety of molecules in solution and this parameter has been shown to be robust descriptor of hydrogen atom transfer (HAT) and proton-coupled electron transfer (PCET) reactivity.[47,49–53] Furthermore, the utility of BDFEs as a descriptor of material bond strengths has already been demonstrated by our group in a recent study of $Ni(OH)_2$ electrodes.[54] Use of these values allows connections to the surface science literature as BDFEs are directly related to the hydrogen adsorption free energies by combination with the free energy of H_2 homolysis.[48,55]

Herein, we report measurements of equilibria between colloidal ceria nanoparticles and various PCET reagents, as a new method, to provide the first experimentally determined BDFEs for surface O–H bonds in colloidal nanoceria, or any colloidal metal oxide nanoparticle. While there have been many studies of the reaction chemistry of metal oxide nanoparticle suspensions,[56–65] it is only recently that PCET reactions have been emphasized.[9,66,67] Our previous study demonstrated that nanoceria colloids react with a wide range of PCET reagents.[68] We show here that reactions between nanoceria and a PCET reagent can reach an equilibrium state where the thermodynamic affinity for a hydrogen atom, or BDFE, is equal between the two species. Interestingly, we observe that these BDFEs are significantly tuned by the redox state of the nanoceria. The implications of this relationship and these values for the rational design of nanoceria catalysts are discussed. More generally, this work opens the door to many more experimental studies of hydrogen adsorption free energies at oxide solid/solution interfaces, which are important in fields including catalysis, electrocatalysis, reaction chemistry, corrosion, geochemistry, nanomedicine, and as benchmarks for computational studies.

Results

This study demonstrates a novel and general method for determining the bond strengths between hydrogen and metal oxide nanoparticles using oleate-capped cerium oxide nanoparticle colloids (OLE-Ce) in low-polarity organic solvents (Supporting Information, Section S1). The majority of experiments were performed in tetrahydrofuran (THF) with an OLE-Ce batch designated **Ce-1**, in which nanoparticles had an average diameter (d) of 1.8 ± 0.2 nm by transmission electron microscopy (TEM) (Section S2). Comparative studies were done with a second batch of OLE-Ce prepared in the same fashion (**Ce-2**, $d = 1.9 \pm 0.3$ nm), and on a larger OLE-Ce colloid (**Ce-L**, $d = 4.0 \pm 0.4$ nm). Experiments involved chemical reactions of these OLE-Ce colloids with soluble small molecules that can donate or accept hydrogen atoms – mostly 1,4-hydroquinones and their corresponding quinones. These PCET reagents were chosen because they have a variety of average O–H BDFEs and they are poor ligands for nanoceria.[55,68] Reactions were done in mixtures of THF-d_8 and proteo-THF over a period of days at room temperature, and organic products were quantified by integration of peaks in the solvent-suppressed ^{1}H NMR spectra using 1,3,5-trimethoxybenzene (TMB) as an internal standard (Sections S1.4 & S6.1). Solutions were also analyzed in air-free quartz capillaries by X-ray absorbance near edge spectroscopy (XANES) at the Ce L_{III}-edge before and after reactions, to obtain the ratio of Ce^{3+} to Ce^{4+} ions in the material (Section S3). For as-prepared **Ce-1**, the %Ce^{3+} is 29.5% by XANES.

Throughout this work, BDFE values are used as thermochemical metrics of hydrogen atom affinity, where larger values indicate stronger bonds. All of the values used for organic substrates (XH_n) were determined recently by our laboratory, in THF, using open-circuit potential measurements.[55] For reagents where $n > 1$ the reported BDFEs refer to the average of the component BDFEs.

I. Equilibrium Case Study: OLE-Ce and 2,6-dimethyl-1,4-hydroquinone (H_2DMQ)

This section describes detailed ^1H NMR and XANES studies of the reaction between **Ce-1** and 2,6-dimethyl-1,4-hydroquinone (H_2DMQ, BDFE = 64.9 kcal mol^{-1})[55] in THF as a case study for the equilibration strategy (Scheme 1). Reaction progress was monitored with ^1H NMR spectroscopy by quantifying the production of the organic product, in this case 2,6-dimethyl-1,4-benzoquinone (DMQ). Quantification of the product provides a direct measure of the change in $\%Ce^{3+}$ ($\Delta\%Ce^{3+}$) during the reaction, because, as demonstrated below, a general stoichiometric relationship holds (eq 2). Reported values of $\Delta\%Ce^{3+}$ are always relative to the $\%Ce^{3+}$ of the as-prepared sample of OLE-Ce, even if multiple reactions are done in sequence.

$$\mathrm{CeO}_x\mathrm{H}_y + a\mathrm{XH}_n \rightleftharpoons \mathrm{CeO}_x\mathrm{H}_{(y+an)} + a\mathrm{X} \qquad (2)$$

The oxidation of H_2DMQ by as-prepared **Ce-1** was explored in the presence of excess reducing equivalents (two per molecule of H_2DMQ) as compared to potential oxidizing equivalents (the number of Ce atoms). Although the concentration of cerium atoms ([Ce]) should be limiting in the reaction with H_2DMQ, reduction of **Ce-1** was observed to plateau at $\Delta\%Ce^{3+} \approx 33\%$, after roughly 3 days (Figure 1A). This value is well below the $\Delta\%Ce^{3+}$ expected for a stoichiometric reaction (see below), and therefore suggested that an equilibrium state was reached. To test this hypothesis, **Ce-1** was first reduced to $\Delta\%Ce^{3+} \approx 36\%$ by using a sub-stoichiometric amount of the more reducing 1,8-dichloro-9,10-dihydroanthraquinone (H_2DCAQ, BDFE = 55.4 kcal mol^{-1})[55]. In this reaction H_2DCAQ is quantitatively oxidized to the quinone. The reduced colloid was then exposed to excess DMQ (Scheme 1 in the reverse direction). Reduction of DMQ to H_2DMQ was observed in initial time points, but then plateaued at $\Delta\%Ce^{3+} \approx 28\%$. The observation of reactions in both directions supports the initial conclusion of achieving equilibrium states. The plateau value of $\Delta\%Ce^{3+}$ was somewhat higher in the oxidation of H_2DMQ than in the reduction of DMQ (Figure 1A), as discussed below.

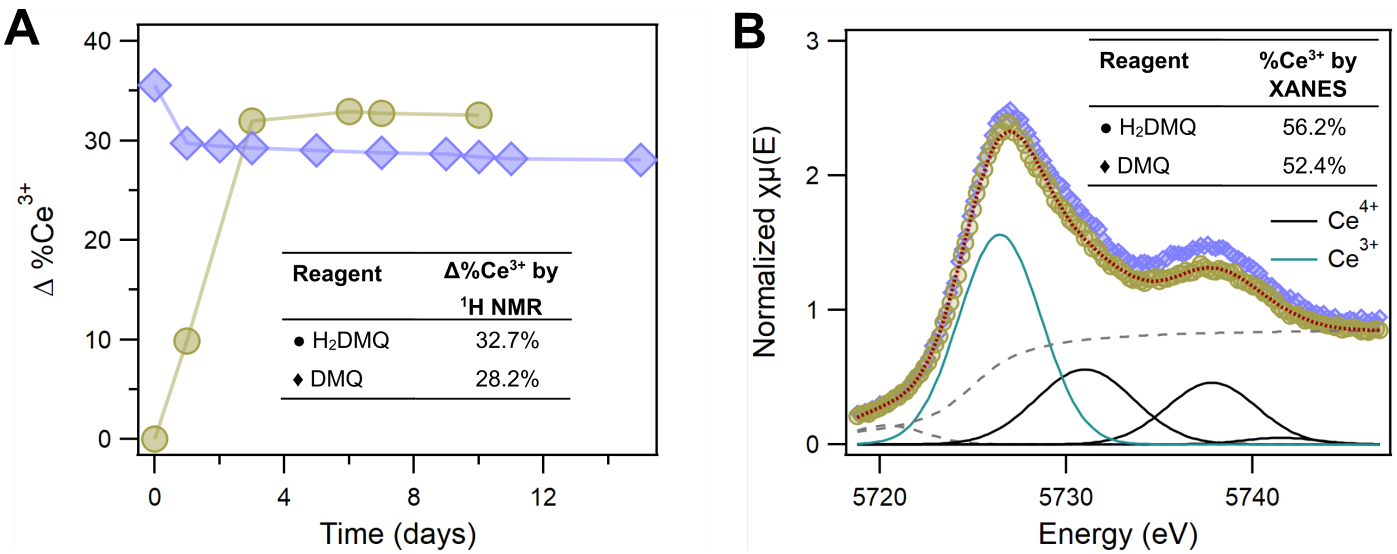

Figure 1. (**A**) Δ%Ce^{3+} values plotted as a function of reaction time, determined by quantitation of the organic products by ^{1}H NMR spectroscopy. The oxidation of H$_2$DMQ (gold) by **Ce-1** and the reduction of DMQ by pre-reduced **Ce-1** (purple) are shown. Uncertainties in the Δ%Ce^{3+} values are roughly the vertical size of the symbols. Values in the table (±2%) are the averages of all Δ%Ce^{3+} values in the plateau region. Δ%Ce^{3+} values were corroborated by (**B**) XANES data of the equilibrated suspensions in THF (same color scheme as Figure 1A). A fit for the spectrum of **Ce-1**/H$_2$DMQ (red, dotted) is included, together with contributions from Ce^{3+} (teal), Ce^{4+} (black), and background / pre-edge contributions (gray, dashed). For the oxidation of H$_2$DMQ by **Ce-1,** [Ce] = 9.0 mM, [H$_2$DMQ] = 6.3 mM, and [TMB] = 7.5 mM. For the reduction of DMQ, **Ce-1** was first reduced by adding a sub-stoichiometric amount of H$_2$DCAQ and waiting until it had all been consumed before adding DMQ; [Ce] = 9.1 mM, [DMQ] = 4.3 mM, and [TMB] = 7.4 mM. As in (**A**), the estimated uncertainties are ≤ ±2% in %Ce^{3+}.

XANES data collected for these colloidal samples at the Ce L$_{III}$-edge provided a direct measure of the absolute %Ce^{3+} (rather than the change, Δ%Ce^{3+}, from ^{1}H NMR data and eq 2). As reported previously, XANES spectra were fit to multiple transitions originating from either Ce^{3+} or Ce^{4+}.[68] In short, absorbance at the rising edge is primarily attributed to a transition from the Ce^{3+} state, while absorbance at higher energies is assigned to multiple transitions from Ce^{4+} states.[69–71] Deconvolution of contributions from Ce^{3+} and Ce^{4+} states in XANES spectra provide a quantitative measure of the absolute %Ce^{3+} of OLE-Ce (Section S3). These experiments again showed that reactions of H$_2$DMQ and DMQ with **Ce-1** and pre-reduced **Ce-1**, respectively, gave fairly similar %Ce^{3+} values (Figure 1B). In both cases, the %Ce^{3+} values were significantly higher than that measured for as-prepared **Ce-1**, %Ce^{3+} = 29.5%.

The final %Ce^{3+} values for reactions between **Ce-1** and either H$_2$DMQ or DMQ (starting at opposite sides of Scheme 1) show a consistent difference by both XANES and ^{1}H NMR. By both measures the reaction with H$_2$DMQ gives a higher %Ce^{3+} than the reaction with excess DMQ. This discrepancy falls outside of the uncertainties, which we estimate to be ≤ ±2% in %Ce^{3+} for both ^{1}H NMR and XANES. Such a discrepancy is actually *expected* for an equilibrium state, because of the excess of the organic reagent that was used in each case. The law of mass action (Le Chatelier's principle) dictates that **Ce-1** will be more reduced when an excess of the H_2DMQ reductant was used, and more oxidized in the presence of an excess of the DMQ oxidant. This is what is observed by both ^{1}H NMR and XANES (Figure 1). Together, these data show that the $2e^-/2H^+$ transfer between **Ce-1** and the H_2DMQ/DMQ redox couple reaches equilibrium.

At equilibrium the overall PCET reaction is isoergic by definition, and therefore the BDFE of **Ce-1** ($BDFE_{Ce}$) must be equal to the "concentration-adjusted BDFE" ($BDFE_{adj}$) of H_2DMQ. The $BDFE_{adj}$ is used because the concentrations of H_2DMQ and DMQ in solution modulate their hydrogen atom affinity, per Le Chatelier's principle. Just as the thermodynamic proton-donor ability of a protic acid depends on the [HA]/[A^-] ratio, the ability of the H_2DMQ to donate hydrogen atoms depends on the [H_2DMQ]/[DMQ] ratio. This change in driving force will necessarily shift the position of the equilibrium measured. The $BDFE_{adj}$ is given quantitatively by a version of the Nernst equation (eq 3), where the constant is 2.303RT at 298 K in kcal mol^{-1}.[55]

$$BDFE_{adj}(XH_n) = BDFE(XH_n) - \frac{1.364\ kcal\ mol^{-1}}{n}\log\left(\frac{[XH_n]}{[X]}\right) \tag{3}$$

Application of eq 3 for the equilibria established between H_2DMQ/DMQ and **Ce-1** gives $BDFE_{Ce}$ = 64.6 kcal mol^{-1} when $\Delta\%Ce^{3+} = 32.7\%$ and 65.6 kcal mol^{-1} when $\Delta\%Ce^{3+} = 28.2\%$. We estimate the uncertainty between $BDFE_{Ce}$ values to be ±0.3 kcal mol^{-1} based on the accuracy of equilibrium positions from the NMR quantitation. The difference in BDFEs for the two equilibrated samples falls outside of the relative uncertainties, thereby confirming the expectation that more reduced ceria nanoparticles form a weaker bond to hydrogen (lower BDFE).

II. Expansion of Equilibrium Method to Other PCET Reagents

The equilibrium method described above was expanded to 1,1-diphenyl-2-picrylhydrazine (DPPH-H, BDFE = 73.5 kcal mol^{-1}), 1,4-hydroquinone (H_2BQ, BDFE = 67.4 kcal mol^{-1}), 1,4-dihydroxynaphthalene (H_2NQ, BDFE = 62.7 kcal mol^{-1}), and 2,7-di-*tert*-butyl-1,4-dihydroxynaphthalene (H_2DTNQ, BDFE = 61.5 kcal mol^{-1}).[55] The BDFEs of these substrates span 12.0 kcal mol^{-1} (Scheme 2).[55] In all cases mass balance of organic products and reagents was maintained during ^{1}H NMR time courses (Figure S24D), and equilibrium states were reached with **Ce-1** when approached through reaction with either the oxidized or reduced form of the PCET reagent (Section S6). Further generalization of these studies to **Ce-2** and **Ce-L** demonstrated the formation of equilibrium states with the same PCET reagents (Table 1). All of the values in Table 1 include the Nernstian corrections for the [XH_n]/[X] ratios, eq 3. For all substrates, the results of each repeated experiment are given (instead of averaged) because each equilibrium state is slightly different due to differing reagent concentrations (Table S5).

Scheme 2. PCET Reagent Structures and Avg. X-H BDFEs in kcal mol^{-1}.[55]

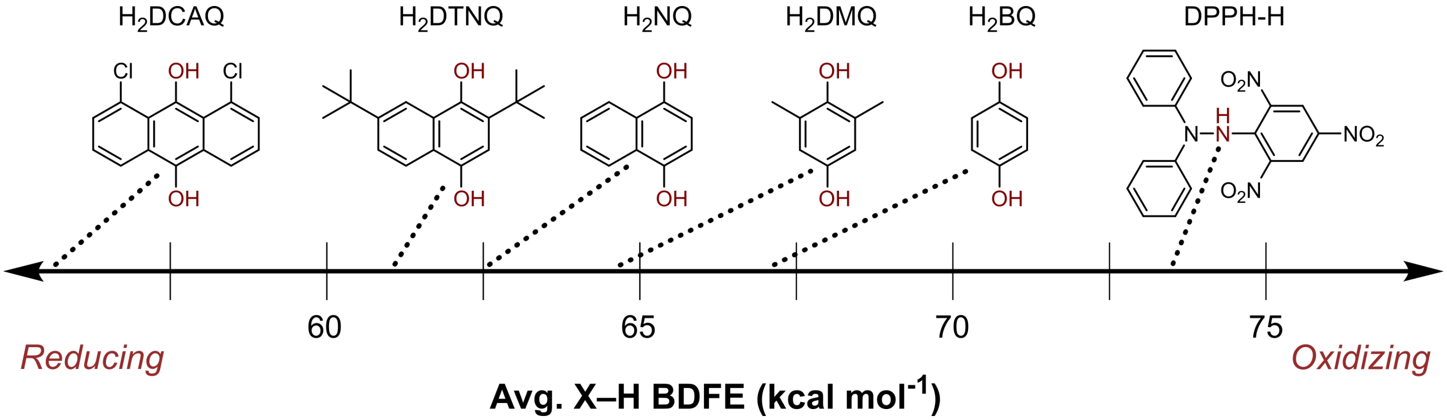

Since the mass balance and reversibility of eq 2 are followed in these reactions (see below), the Δ%Ce^{3+} values determined by ^1H NMR can be made absolute by using a XANES %Ce^{3+} value as a reference point. The XANES value for the **Ce-1**/H_2DMQ equilibrated sample was chosen as the reference since the reaction shows facile kinetics, the same sample has been measured by both XANES and ^1H NMR, and the equilibrium %Ce^{3+} value lies close to the center of the range explored in these studies. This final reason is important because, while XANES is a direct measure of the %Ce^{3+}, the spectral fitting procedure assumes that the peaks shapes for the Ce^{3+} and Ce^{4+} contributions to the spectrum remain constant over the entire range of %Ce^{3+}. A generalized %Ce^{3+} anchor of 23.5% for as-prepared **Ce-1** was determined from the %Ce^{3+} reference point measured by XANES and Δ%Ce^{3+} by ^1H NMR for **Ce-1**/H_2DMQ (Figure 1). Similar procedures were also applied to give anchor values for as-prepared **Ce-2** (24.8%) and **Ce-L** (10.8%). For the remainder of this report, all quoted %Ce^{3+} values were determined by ^1H NMR using these anchor values unless otherwise stated.

Table 1. OLE-Ce Colloid Equilibrium States and BDFEs.[a]

Reagent	%Ce^{3+}	BDFE$_{Ce}$	Reagent	%Ce^{3+}	BDFE$_{Ce}$	Reagent	%Ce^{3+}	BDFE$_{Ce}$
DTNQ [b]	72.6	62.3	H$_2$BQ [c]	43.6	66.9	H$_2$BQ [d]	44.2	67.0
H$_2$DTNQ [c]	72.2	61.3	H$_2$BQ [c]	42.7	66.9	H$_2$BQ [d]	44.1	67.0
H$_2$DTNQ [c]	72.2	61.5	BQ [b]	36.1	68.0	DPPH [d]	15.1	72.5
DTNQ [b]	70.3	62.6	BQ [b]	36.0	68.2	DPPH [d]	14.1	73.1
DTNQ [b]	66.8	62.2	DPPH [c]	18.0	74.2	H$_2$DTNQ [e]	20.6	60.7
NQ [b]	63.6	63.4	DPPH [c]	17.5	74.3	H$_2$NQ [e]	20.1	61.9
H$_2$NQ [c]	62.2	62.5	H$_2$DTNQ [d]	65.6	61.4	H$_2$DTNQ [e]	20.0	60.8
H$_2$NQ [c]	61.5	62.7	H$_2$DTNQ [d]	64.2	61.4	DTNQ [f]	19.4	61.9
NQ [b]	60.1	63.6	H$_2$NQ [d]	59.8	62.5	H$_2$NQ [e]	18.5	61.9
NQ [b]	59.7	63.6	H$_2$NQ [d]	59.3	62.5	H$_2$DMQ [e]	17.6	64.0
H$_2$DMQ [c]	56.2	64.6	H$_2$NQ [d]	59.1	62.5	H$_2$DMQ [e]	16.6	64.0
H$_2$DMQ [c]	53.2	64.6	H$_2$DMQ [d]	53.4	64.6	H$_2$BQ [e]	14.6	66.3
DMQ [b]	52.6	65.5	H$_2$DMQ [d]	52.9	64.6	H$_2$BQ [e]	14.1	66.3
DMQ [b]	51.7	65.6	H$_2$DMQ [d]	52.6	64.6	DPPH [e]	8.4	73.4

[a] %Ce^{3+} from ^{1}H NMR data benchmarked to XAS results for OLE-Ce/H$_2$DMQ. BDFE$_{Ce}$ is equal to the BDFE$_{adj}$ from eq 3. BDFEs in kcal mol^{-1} with relative uncertainties of ±0.3 kcal mol^{-1}. [b] Reacted with **Ce-1** that was first reduced with H$_2$DCAQ. [c] Reacted with **Ce-1**. [d] Reacted with **Ce-2**. [e] Reacted with **Ce-L** with equilibrium plateau at ≥24 days. [f] Reacted with **Ce-L** that was first reduced with H$_2$DCAQ.

Successful equilibrium studies required PCET reagents to show mass balance in terms of reagent consumed and product formed (eq 2), and to have a small enough kinetic barrier for the reaction with OLE-Ce to allow for quantification of reaction progress. Substrates which were explored but did not meet these criteria include 2,2,6,6-tetramethylpiperidin-1-yl)oxyl (TEMPO) and 2,6-di-tert-butyl-4-methoxy phenoxyl radical, both of which reacted on timescales too slow for reasonable measurement (no reaction completion after >1 month). Additionally, reactions between *meta*-chloroperbenzoic acid (*m*CPBA) and OLE-Ce were facile but did not show mass balance (Section S4).

Equilibria between OLE-Ce and hydroquinones were also studied under alternative solvent conditions (Section S8). In a THF solution containing 0.1 M tetrabutylammonium hexafluorophosphate electrolyte, the equilibrium position measured for the H$_2$BQ/**Ce-1** reaction was nearly unchanged from that in pure THF. Additionally, changing the solvent from THF to lower polarity solvents, such as toluene-*d*$_8$, led to greater reduction of OLE-Ce in reactions with H$_2$DMQ. These results indicate that the reactions do not involve any significant change in the charge of the nanoparticles, as is discussed further below.

We also explored potential perturbations of the H_2DMQ/**Ce-1** equilibrium by excess cerium(III) oleate ($Ce(OLE)_3$), oleic acid, tetrabutylammonium oleate (TBA^+OLE^-), and H_2O. Addition of H_2O and $Ce(OLE)_3$ had no effect on the equilibrium position (Table S7). Addition of TBA^+OLE^- lead to a loss in H_2DMQ mass balance over time, deprotonation of H_2DMQ, and halted oxidation to DMQ. Finally, addition of oleic acid led to greater oxidation of H_2DMQ, as well as the production of $Ce(OLE)_3$ (Figure S29). Analyses of these equilibrium shifts are presented below.

III. Validation of Mass Balance (Eq 2) Across the Full Range of Accessible %Ce^{3+}

Previous XANES studies in our group have demonstrated that a single batch of similarly prepared oleate-capped cerium oxide nanoparticles accessed a wide range of %Ce^{3+}, from ca. 18% to 67%.[68] The range of %Ce^{3+} accessed in reactions with PCET reagents is valuable as it provides a lower limit for the average number of redox-active sites per OLE-Ce nanoparticle. For **Ce-1** the range was measured through reactions with well-behaved highly-oxidizing and highly-reducing organic PCET reagents. The strongest reductant used in these studies was H_2DCAQ, while the strongest well-behaved oxidant used was 2,2-diphenyl-1-picrylhydrazyl (DPPH), which reduces to DPPH-H.

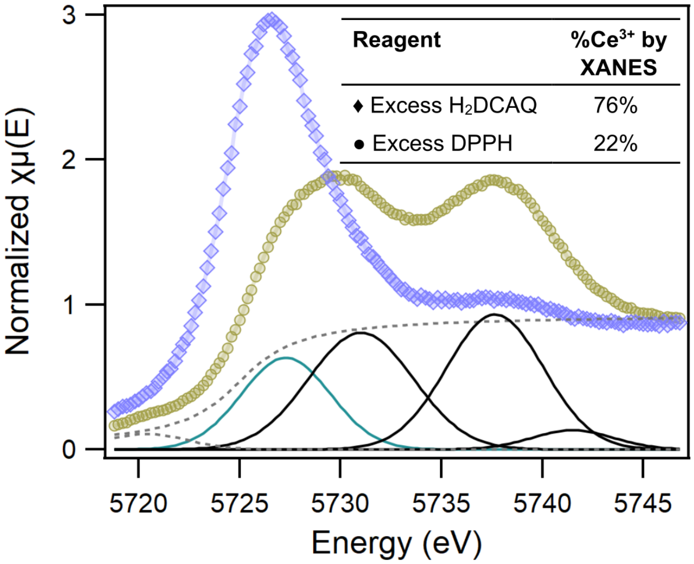

Figure 2. XANES spectra of reactions of **Ce-1** with either excess H_2DCAQ (purple, diamonds) or excess DPPH (gold, circles) in THF. Fits for the spectrum of **Ce-1** / DPPH are included with contributions from Ce^{3+} (teal), Ce^{4+} (black), and background / pre-edge contributions (gray, dashed).

In reactions with excess H_2DCAQ or with excess DPPH, XANES measurements of the %Ce^{3+} of **Ce-1** vary from 22 – 76% (Figure 2), a range of 54%. This range is consistent with the range in %Ce^{3+} observed by ^{1}H

NMR ($\Delta\%Ce^{3+} = 58 \pm 2\%$). The NMR value has greater uncertainty due to side reactions which occur between highly reduced **Ce-1** and H_2DCAQ (Section S4.1). The reversibility of these redox transformations was also tested by subjecting **Ce-1** to repeated oxidation and reduction cycles with DPPH and H_2DCAQ. These experiments show a nearly identical relationship between expected and measured $\%Ce^{3+}$, demonstrating that these redox reactions are quantitative and highly reversible (Figure 3). This assertion is further supported by ^1H NMR studies of the **Ce-1** ligand sphere, which showed reversible changes in the NMR integrals for bound oleate and H_2O upon reduction and re-oxidation (Section S4). Dynamic light scattering (DLS) studies of **Ce-2** also indicate that the size and dispersity of the colloid remain constant with reduction (Figure S8). These investigations confirm the reversibility of redox reactions at OLE-Ce colloids and the validity of eq 2 across the full range of $\%Ce^{3+}$ accessed in these studies.

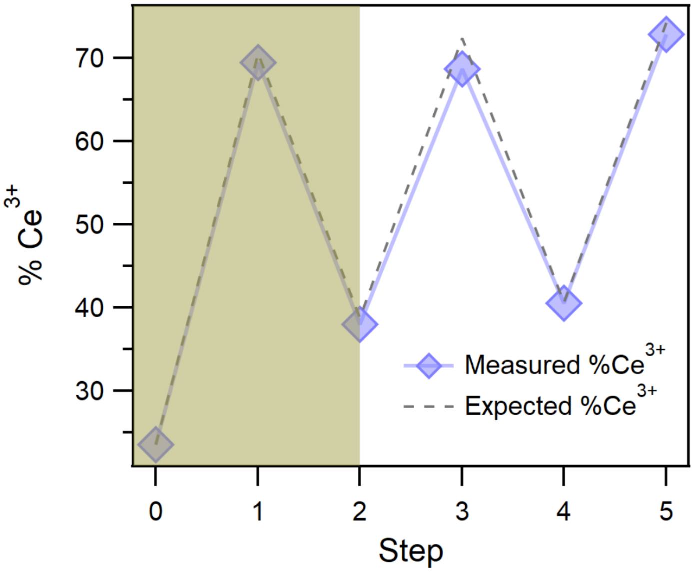

Figure 3. Redox cycling of **Ce-1** using H_2DCAQ as the reductant and DPPH as the oxidant. NMR samples were prepared using stock solutions of H_2DCAQ and DPPH in THF-d_8. The traces for the observed (purple) and expected (gray) changes in $\%Ce^{3+}$ are shown. Expected $\%Ce^{3+}$ was determined by quantifying organic products produced (and therefore $\Delta\%Ce^{3+}$) for the first additions of H_2DCAQ and DPPH stock solutions shown in the shaded region (gold) of the graph. Uncertainties are similar to the size of the symbols.

Discussion

I. OLE-Ce BDFE Trends

Equilibrium states are reached between OLE-Ce and a variety of PCET reagents, providing a direct measure of the hydrogen atom affinity of the ceria nanoparticles, the $BDFE_{Ce}$, at various values of $\%Ce^{3+}$ (Table 1). A plot of these data shows a roughly linear inverse correlation for the **Ce-1** and **Ce-2** samples (Figure 4, blue circles and green stars), where more reduced ceria nanocrystals – higher %Ce^{3+} – have weaker bonds to hydrogen – lower BDFE$_{Ce}$. The larger **Ce-L** nanocrystals also show an inverse linear correlation (Figure 4, orange triangles), but the correlation for **Ce-L** is steeper and shifted to lower values of %Ce^{3+}. These negative correlations match the general chemical intuition that reducing OLE-Ce colloids should weaken their ceria–H bonds. The observation of similar relationships for all three batches of nanoceria, despite their differences in size, highlights the generality of this result. We also note that these plots of BDFE$_{Ce}$ vs. %Ce^{3+} are significantly less linear without the Nernstian correction for the concentrations of the PCET reagents (Figure S26).

Remarkably, the BDFE$_{Ce}$ of **Ce-1** is tuned over 13.0 kcal mol^{-1} (0.56 eV) with changes in the %Ce^{3+}. Similar ranges in BDFE$_{Ce}$ are observed for **Ce-2** and **Ce-L** (Table S5). For **Ce-1**, this enormous range in BDFE$_{Ce}$ occurs over a change in %Ce^{3+} from 17.5% to 72.2%. This variation in BDFE$_{Ce}$ with %Ce^{3+} is too large to be explained solely by a Le Chatelier or mass-action effect, which would predict a change of only 0.6 kcal mol^{-1} for this change in %Ce^{3+}.[i] This effect is even more pronounced for the larger **Ce-L** colloid, where the same variation in BDFE$_{Ce}$ occurs over a change in %Ce^{3+} of only 12%. The difference in the slopes of these correlations is discussed below.

---

[i] A Nernstian relationship where the BDFEs vary according to –RT[log(%Ce^{3+}/%Ce^{4+})] would predict a variation of 0.64 kcal mol^{-1} for a change of %Ce^{3+} from 17.5% to 72.2%:

$$-0.001987(298)\left[\log\left(\frac{17.5}{(100-17.5)}\right)-\log\left(\frac{(72.2)}{(100-72.2)}\right)\right] = 0.64\ \text{kcal mol}^{-1}$$

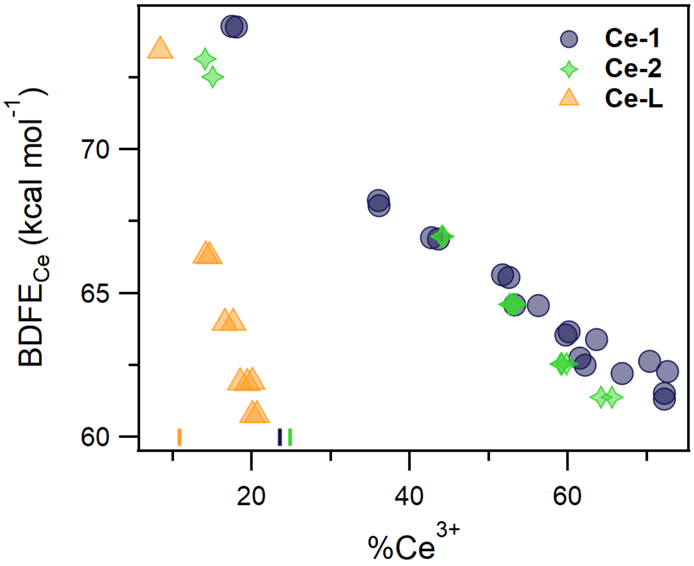

Figure 4. Plot of BDFE$_{Ce}$ vs. the %Ce^{3+} of various OLE-Ce colloids at equilibrium with different organic reagents. The data (from Table 1) are for **Ce-1** (blue circles), **Ce-2** (green stars), and **Ce-L** (orange triangles) equilibrium states. Colored tick marks on the x-axis denote the anchor %Ce^{3+} values of as-prepared OLE-Ce colloids.

II. OLE-Ce Active Site Location and Structure:

The data presented above demonstrate that OLE-Ce can reversibly store and release a large number of hydrogen atom equivalents, but they do not reveal the location and structure of the added H$^{\bullet}$ – the relevant active site(s). A detailed description of the structure of these oleate-capped and very small nanocrystals (ca. 4 unit cells across) is beyond the scope of this study. However, the results do provide insight into the specific questions of what kinds of bonds are formed and whether reduction occurs primarily at surface sites or throughout the bulk of the nanocrystal.

The issue of surface vs. bulk reduction was investigated by examining how the maximum loading of hydrogen atoms was affected by nanoparticle size. By XANES, the smaller **Ce-1** particles (d = 1.8 nm) could be reduced as far as 76% in %Ce^{3+}, while the larger **Ce-L** (d = 4.0 nm) could be reduced to only 30% (Table S4). This suggests a surface-confined process, because the larger particles have a smaller fraction of surface cerium ions (Table S1). To quantitatively probe the hypothesis that reduction occurs primarily at the surface, the number of surface cerium sites was estimated by two methods. In the first, the nanoparticle was treated as a sphere and its surface as a shell, while in the second the number of surface cerium atoms was estimated based on the reported faceting of uncapped 3 – 10 nm cerium oxide nanoparticles.[72] The sphere method estimates that the proportion of surface cerium atoms for **Ce-1** and **Ce-L** are 80-89% and 47-55% respectively, while the facet method estimates

76 – 95% and 35 – 42%, based on the size distributions determined from TEM images (Section S2). While both of these methods require significant assumptions, the differences in proportions of surface cerium atoms between the two sizes of OLE-Ce are larger than the uncertainties. These estimates indicate a surface-confined process, which is consistent with the literature on H_2 reduction of ceria.[26,29,45,73] They imply that a large fraction of surface cerium ions can be reduced in these reactions, while the cerium ions in the core of the nanocrystals are much more resistant to reduction.

Scheme 3. Possible PCET Reactions at Nanoceria Surfaces.

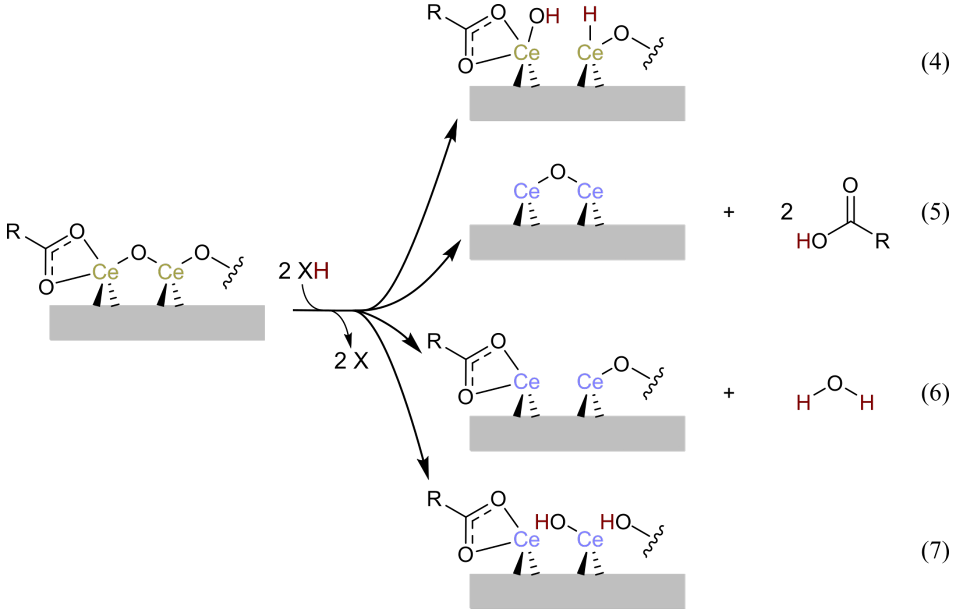

Transfer of hydrogen atoms from the organic reagents to the ceria surface could in principle form water, form oleic acid from surface oleate groups, form surface hydroxides, or form cerium hydrides (Scheme 3). The formation of cerium hydrides has recently been proposed in gas-solid hydrogenation reactions, at high temperatures or with heat-treated ceria, and in reactions with borane reagents.[74–77] However, our observation of %Ce^{3+} increasing upon addition of hydrogen atom donors is incompatible with the proposed mechanisms of Ce–H formation given the BDFEs of the reductants used in these studies (eq 4). Nanoceria mechanisms involving the formation of either oleate/oleic acid or H_2O (eqs 5,6) can also be ruled out (Section S8). Addition of 3Å sieves, which should remove free H_2O in THF, does not affect the ability to reversibly change the %Ce^{3+} of **Ce-1** (Figure S12), and the measured changes in oleic acid concentrations during the reactions are not consistent with the stoichiometric relationship in eq 5. Addition of excess oleic acid leads to greater oxidation of H_2DMQ by **Ce-1**, and addition of TBA^+OLE^- shuts down reactivity. These observations are contradictory to the mechanism shown in eq 5. The increased reactivity of **Ce-1** in the presence of oleic acid occurs concomitantly with the appearance of Ce(OLE)$_3$ in the ^{1}H NMR spectrum. Ce(OLE)$_3$ does not grow in the ^{1}H NMR spectrum if oleic acid is not added in excess, and addition of only Ce(OLE)$_3$ does not perturb the equilibrium position of H$_2$DMQ/**Ce-1** (Figure S29). In light of these results, we propose that oleic acid protonates surface Ce^{3+} ions to form solution-phase Ce(OLE)$_3$, thereby generating more active ceria surface and boosting apparent reactivity.

By process of elimination, it is most likely that OLE-Ce colloids react to form hydroxyl groups (eq 7). Although we were unable to directly verify this structure for OLE-Ce, other reports have observed or predicted surface hydroxyl groups on ceria under other conditions.[26,29,44,78–82] Because the redox chemistry occurs primarily at the surface cerium ions (see above), and the conversion of oxide to hydroxide provides the local charge balance for the reduction to Ce^{3+}, it is most likely that the hydroxide groups formed are also at the surface. As a result, we conclude that the relevant thermodynamic predictor of PCET reactivity at OLE-Ce is the BDFE of its surface O–H bonds.

We now revisit the correlation of BDFE$_{\mathrm{Ce}}$ with %Ce^{3+}, in light of the conclusions that the transfer of hydrogen atoms to the ceria nanocrystals forms surface Ce^{3+} and hydroxide ions. By using the %Ce^{3+} metric, Figure 4 implicitly assumes that all cerium atoms in OLE-Ce are active. Since the majority of redox activity comes from surface cerium atoms, a more appropriate analysis would only use the fraction of cerium atoms at the nanocrystal surface. To estimate this fraction, we use the facet method described above with the average diameters from TEM measurements. These indicate that roughly 85% of the cerium atoms are at the surface for **Ce-1**, 80% for **Ce-2** and 39% for **Ce-L** (Section S2.2). With the assumption that the measured changes in %Ce^{3+} occur only at surface sites, these values provide estimates of the percentage of surface cerium atoms that are Ce^{3+} (%Surface-Ce^{3+}). Replotting the data as BDFE$_{\mathrm{Ce}}$ vs. %Surface-Ce^{3+} significantly coalesces the relationships observed for the three OLE-Ce batches (Figure 5). The shaded regions in Figure 5 are estimates of the uncertainties in %Surface-Ce^{3+} calculated from 1σ variance in the average diameters by TEM. When accounting for these uncertainties, the data for **Ce-L** remains distinct from that for **Ce-1** and **Ce-2**, an observation that future work will need to examine. Still, the closer agreement between the large and small OLE-Ce batches supports the conclusion that redox reactivity occurs primarily at surface sites, as is commonly found for nanoceria.[83,84]

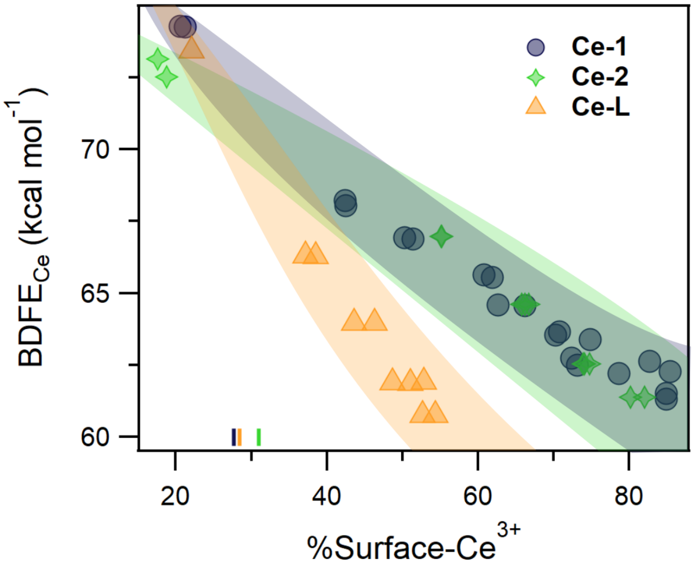

Figure 5. Plot of BDFE$_{Ce}$ (the same data as Figure 4; Table 1) vs. the %Surface-Ce^{3+} for **Ce-1** (blue circles), **Ce-2** (green stars), and **Ce-L** (orange triangles). The %Surface-Ce^{3+} were estimated from the average nanoparticle diameters (*d*) from TEM images, and the shaded regions estimate the uncertainties resulting from the 1σ variance in *d*. Colored tick marks on the x-axis denote the anchor %Surface-Ce^{3+} values of as-prepared OLE-Ce colloids.

III. Physical Models of the BDFE$_{Ce}$ vs. %Surface-Ce^{3+} Relationship and their Implications

The large variation in BDFE$_{Ce}$ with changes in the average redox state of the ceria nanocrystals was unexpected. This section explores plausible physical models of interfacial energetics that could shed light on this variation.

In principle, the linear relationship between BDFE$_{Ce}$ and the "charge added", or %Surface-Ce^{3+}, could be described by a capacitive model, similar to previous studies of ZnO nanoparticles.[85] However, invoking this model is inconsistent with a basic property of capacitive systems: a buildup of electric charge.[ii] The equilibrations above involve the movement of chemical redox equivalents, but as neutral hydrogen atoms. The lack of charge buildup in these reactions is confirmed by the insensitivity of OLE-Ce reduction to the addition of electrolyte or lowering of the solvent dielectric constant (Section S8). As a result, a traditional capacitive model can be ruled out for the data presented above.

A more attractive model comes from surface science where the relationship between hydrogen adsorption energy and surface coverage (θ) has been studied in detail for well-defined metal surfaces using *isotherms*. The

---

[ii] An areal capacitance can be estimated from the ca. 77 Ce atoms per 1.8 nm diameter nanoparticle for **Ce-1** and from the Δ%Ce^{3+} being 54.7% between states spanning 13.0 kcal mol^{-1} (or 564 mV) in BDFE:

Areal Capacitance = q/ΔEA, where q in Coulombs = $(77*0.564*1/(6.24*10^{18}))$ C, ΔE = 0.546 V, and the area of a sphere of radius 0.9 nm is $(4\pi*(0.9*10^{-7})^2)$ cm^2, yielding areal capacitance = 125 μF cm^{-2}.

simplest of these models is the Langmuir isotherm which describes surface adsorbates as an ideal 2D gas, such that the adsorption energy is independent of θ. This treatment is highly analogous to a Nernstian electrochemical dependence. As noted above, the $BDFE_{Ce}$ vs. %Surface-Ce^{3+} in Figure 5 cannot be fit with Langmuirian or Nernstian treatments, which would predict a 20-fold smaller variation in $BDFE_{Ce}$. However, deviations from Langmuirian behavior are well known, and in such cases data are often modeled with the Frumkin isotherm.[86] This applies a linear correction to the Langmuir isotherm, such that the hydrogen adsorption energy at $\theta = 0.5$ is $\mu + 0.5C$ where C designates the magnitude of the linear correction in kcal mol^{-1} (eq 8).

$$BDFE_{Ce} = \mu - 1.364 \times \log\left(\frac{\theta}{1-\theta}\right) + C \times \theta \tag{8}$$

Application of a Frumkin isotherm to the data in Figure 5 leads to good fits (Figure S27). In fits to eq 8, the dependence on θ is dominated by the correction term; for instance, $C \cong 16$ kcal mol^{-1} for **Ce-1** and **Ce-2**.

At present, we have limited insight into the physical basis for the large Frumkin correction required to fit the $BDFE_{Ce}$ vs. Surface-%Ce^{3+} data for OLE-Ce. Frumkin corrections are commonly associated with either interactions between adsorbates or with a distribution of chemically distinct adsorption sites. Either explanation could apply to these ceria nanoparticles based on prior studies. In support of a distribution of chemically distinct active sites, crystallographic analyses of atomically-precise nanoceria clusters demonstrate local distortions in Ce–O bond lengths near Ce^{3+} sites, suggest that Ce^{4+} and Ce^{3+} ions have different ligand preferences, and provide evidence for a localized, or mixed-valence, description of nanoceria electronic structure.[87] Ligand effects are also known for aqueous Ce^{4+} cations, where anion identity is known to have a significant effect on the reduction potential.[88] Furthermore, a computational study of Ce_nO_{2n} nanoclusters, where $n = 12$ and $n = 14$, has shown that the hydrogen adsorption energy can vary by as much as 0.3 eV depending on the adsorption site.[46] However, the continuous linearity of the $BDFE_{Ce}$ vs. %Surface-Ce^{3+} relationship could be suggestive of an adsorbate-interaction model. This is further supported by an *ab initio* study which calls into question the mixed valence description of ceria, and instead suggests greater covalency in the lattice.[89] Additionally, adsorbate interactions have already been invoked to explain the well-studied relationship between ceria nanoparticle size and lattice parameter.[90] Parsing these effects is complex as localized states can also induce adsorbate interactions through lattice strain, an effect that is further heightened for small nanoparticles such as the ones used in these studies. From this perspective, these two models may not be so distinct given that each OLE-Ce colloid has distribution of nanoparticles sizes, a high concentration of edge and corner sites, and a complex distribution of capping ligands.

The *non*-Langmuirian behavior of ceria observed here may be important for improving and understanding its efficacy in applications as a catalyst and catalyst support. A recent report showed that even small changes in %Ce^{3+} (<10%) of a ceria support can induce significant changes in the oxidation state of platinum single-atom catalysts and influence their oxidation activities.[91] Furthermore, the %Ce^{3+} of aqueous nanoceria colloids has been shown to modulate its activity for scavenging reactive oxygen species.[24,25] Related effects are likely relevant to the high temperature (>600 K) oxygen-atom transfer reactivity of ceria, where relationships between oxygen vacancy concentration and oxygen chemical potential are known.[27,40,92,93] The chemical potentials of oxygen (μ_O) and hydrogen ($BDFE_{Ce}$) in ceria are simply related by the addition of water to an oxygen vacancy (Scheme 4);[42] this is the basis of solar-thermal water splitting by CeO_2 and other oxides.[94–96] At the suggestion of a reviewer, we include a plot of our $BDFE_{Ce}$ values measured at room temperature *vs.* the μ_O of bulk ceria at 1,000 °C for the same ratio of reduced active sites (Figure S28).[27,40] Interestingly, a strong negative correlation is observed, consistent with the chemical intuition implied by Scheme 4. While the conditions are very different between these two measurements, this plot demonstrates a clear connection between the low and high temperature reactivity of ceria.

Scheme 4. Relating Oxygen Vacancies and Surface Hydrogen.

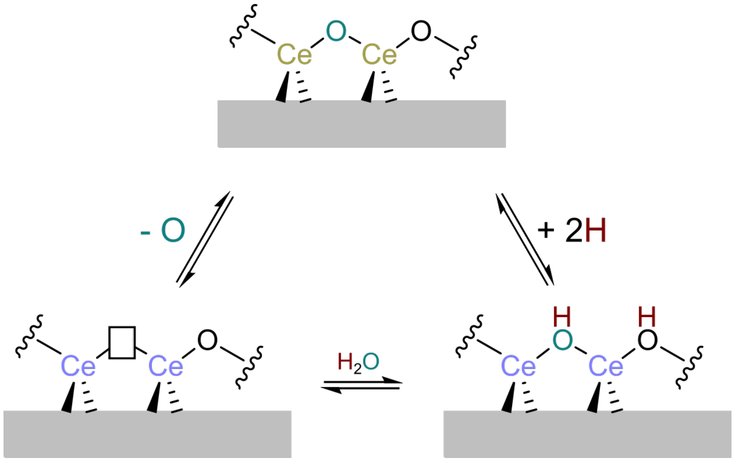

The relationship between $BDFE_{Ce}$ and %Ce^{3+} also has implications for *in silico* studies of hydrogen adsorption at materials which, for the most part, report single values for the hydrogen adsorption energy. In the context of ceria, reported $CeO_2(111)$ surface O–H bond strengths are in the same range as reported here, 62 to 82 kcal mol^{-1}, but they vary between different *in silico* studies. Furthermore, the effect of ceria redox state has not been significantly explored.[29,44,45] Experimental investigations of materials other than ceria have also suggested *ranges* of hydrogen adsorption energies. For example, a similar relationship between hydrogen atom affinity and redox state has been observed for tungsten trioxide,[97] and a recent study of cobalt phosphide from our group also suggests a distribution of BDFEs.[98] Consideration of these ranges in bond strengths will likely have implications for 'volcano plot' analyses that often use a single hydrogen binding energy as the descriptor. Due to the general importance of MO–H bond strengths, we hope that this study will stimulate new computational approaches to understand the relationship between material redox state and bond strength thermochemistry.[99]

Conclusions

We present a novel equilibrium strategy for determining the hydrogen atom affinity of colloidal metal oxide nanoparticles through solution-phase reactivity studies of organic PCET reagents and oleate-capped cerium oxide nanoparticles. On average, nearly 60% of cerium atoms in a 2 nm diameter nanoparticle were shown to be redox active in these PCET reactions. Redox changes across this wide range of $\%Ce^{3+}$ were demonstrated to be reversible through an in-depth accounting of reaction stoichiometries and parallel characterizations of the colloids by ^1H NMR and XANES. The observed reversibility, and other data, show that in these reactions OLE-Ce colloids reach equilibrium states with many of the organic reagents used. Studies of how nanoparticle size affects the position of the equilibrium state demonstrated that the relevant bond on OLE-Ce is surface-confined, and further investigations indicated that the bond is a surface O–H group. On the basis of these findings, we have measured surface O–H BDFEs for colloidal nanoceria, and the first experimental BDFEs for any nanoscale metal oxide. This work demonstrates that the concepts of molecular bond strength thermochemistry can be applied to nanoscale materials to measure their hydrogen atom affinities.

Remarkably, the measured CeO–H BDFEs span 13 kcal mol^{-1} (0.56 eV) and show a linear dependence on the $\%Ce^{3+}$ of the nanocrystals. This broad relationship, which was not previously recognized, can be well described by a Frumkin isotherm that deviates substantially from Langmuirian behavior. The range of BDFEs measured provide important experimental benchmarks for future *in silico* studies and highlight the importance of considering the compositional complexities of nanoceria and many other catalytic and electrocatalytic metal oxide surfaces. Along these lines, we propose that the tunability of $BDFE_{Ce}$ is important to the widespread use of ceria as a catalyst support. These findings should further the design and understanding of ceria-based catalysts and beyond.

Supporting Information

Complete experimental details, procedures and analysis, characterization of nanoparticle colloids and organic reagents, and further experiments which probe the reversibility of redox changes at OLE-Ce and how non-standard solution conditions affect equilibrium states.

Author Information

*Corresponding Author: james.mayer@yale.edu
ORCID:
James M. Mayer: 0000-0002-3943-5250
Rishi G. Agarwal: 0000-0002-5133-0136

Notes

The authors declare no competing financial interest.

Acknowledgements

We thank Dr. Eric Paulson (Yale Chemical and Biophysical Instrumentation Center) for assistance with quantitative ^1H NMR studies and Dr. Tianpin Wu (Argonne National Laboratory Advanced Photon Source) for assistance with XANES. This research used resources of the Advanced Photon Source, a U.S. Department of Energy (DOE) Office of Science User Facility operated for the DOE Office of Science by Argonne National Laboratory under Contract No. DE-AC02-06CH11357. This research was supported by funding from the National Science Foundation under CHE-1609434 and CHE-1904813. R.G.A. acknowledges support from a National Science Foundation Graduate Research Fellowship. H.J.K. acknowledges support by the Arthur Fleischer Award and Richter Summer Fellowship through Yale University.

References

(1) Jackson, S. D.; Hargreaves, J. S. J. *Metal Oxide Catalysis*, 1st ed.; Wiley, 2008. https://doi.org/10.1002/9783527626113.

(2) Fierro, J. L. G. *Metal Oxides: Chemistry and Applications*, 0 ed.; CRC Press, 2005. https://doi.org/10.1201/9781420028126.

(3) Védrine, J. C. *Metal Oxides in Heterogeneous Catalysis*; Elsevier, 2018. https://doi.org/10.1016/C2016-0-01790-4.

(4) Pourbaix, M. *Atlas of Electrochemical Equilibria in Aqueous Solutions*; National Association of Corrosion Engineers: Houston, Texas, 1974.

(5) Stumm, W.; Morgan, J. J. *Aquatic Chemistry: Chemical Equilibria and Rates in Natural Waters*, 3rd ed.; Wiley-Interscience: New York, 1995.

(6) Rodríguez, J. A.; Fernández-García, M. *Synthesis, Properties, and Applications of Oxide Nanomaterials*; John Wiley & Sons, Inc., 2006.

(7) Bard, A. J. Inner-Sphere Heterogeneous Electrode Reactions. Electrocatalysis and Photocatalysis: The Challenge. *J. Am. Chem. Soc.* **2010**, *132* (22), 7559–7567. https://doi.org/10.1021/ja101578m.

(8) Wöll, C. Hydrogen Adsorption on Metal Oxide Surfaces: A Reinvestigation Using He-Atom Scattering. *J. Phys. Condens. Matter* **2004**, *16* (29), S2981–S2994. https://doi.org/10.1088/0953-8984/16/29/012.

(9) Schrauben, J. N.; Hayoun, R.; Valdez, C. N.; Braten, M.; Fridley, L.; Mayer, J. M. Titanium and Zinc Oxide Nanoparticles Are Proton-Coupled Electron Transfer Agents. *Science* **2012**, *336* (6086), 1298. https://doi.org/10.1126/science.1220234.

(10) Van de Walle, C. G.; Neugebauer, J. HYDROGEN IN SEMICONDUCTORS. *Annu. Rev. Mater. Res.* **2006**, *36* (1), 179–198. https://doi.org/10.1146/annurev.matsci.36.010705.155428.

(11) Fung, V.; Hu, G.; Wu, Z.; Jiang, D. Hydrogen in Nanocatalysis. *J. Phys. Chem. Lett.* **2020**, *11* (17), 7049–7057. https://doi.org/10.1021/acs.jpclett.0c01783.

(12) Campbell, C. T.; Sellers, J. R. V. Enthalpies and Entropies of Adsorption on Well-Defined Oxide Surfaces: Experimental Measurements. *Chem. Rev.* **2013**, *113* (6), 4106–4135. https://doi.org/10.1021/cr300329s.

(13) Campbell, C. T.; Mao, Z. Chemical Potential of Metal Atoms in Supported Nanoparticles: Dependence upon Particle Size and Support. *ACS Catal.* **2017**, *7* (12), 8460–8466. https://doi.org/10.1021/acscatal.7b03090.

(14) Seh, Z. W.; Kibsgaard, J.; Dickens, C. F.; Chorkendorff, I.; Nørskov, J. K.; Jaramillo, T. F. Combining Theory and Experiment in Electrocatalysis: Insights into Materials Design. *Science* **2017**, *355* (6321), eaad4998. https://doi.org/10.1126/science.aad4998.

(15) Quaino, P.; Juarez, F.; Santos, E.; Schmickler, W. Volcano Plots in Hydrogen Electrocatalysis – Uses and Abuses. *Beilstein J. Nanotechnol.* **2014**, *5*, 846–854. https://doi.org/10.3762/bjnano.5.96.

(16) Nørskov, J. K.; Bligaard, T.; Logadottir, A.; Kitchin, J. R.; Chen, J. G.; Pandelov, S.; Stimming, U. Trends in the Exchange Current for Hydrogen Evolution. *J. Electrochem. Soc.* **2005**, *152* (3), J23. https://doi.org/10.1149/1.1856988.

(17) Schmickler, W.; Trasatti, S. Comment on "Trends in the Exchange Current for Hydrogen Evolution" [J. Electrochem. Soc., 152, J23 (2005)]. *J. Electrochem. Soc.* **2006**, *153* (12), L31. https://doi.org/10.1149/1.2358294.

(18) Samorjai, G. A.; Li, Y. Thermodynamics of Adsorbed Monolayers. In *Introduction to Surface Chemistry and Catalysis*; John Wiley & Sons, Inc.: New York, 2010; pp 313–323.

(19) Ganduglia-Pirovano, M. V. The Non-Innocent Role of Cerium Oxide in Heterogeneous Catalysis: A Theoretical Perspective. *Catal. Today* **2015**, *253*, 20–32. https://doi.org/10.1016/j.cattod.2015.01.049.

(20) Kibsgaard, J.; Tsai, C.; Chan, K.; Benck, J. D.; Nørskov, J. K.; Abild-Pedersen, F.; Jaramillo, T. F. Designing an Improved Transition Metal Phosphide Catalyst for Hydrogen Evolution Using Experimental and Theoretical Trends. *Energy Environ. Sci.* **2015**, *8* (10), 3022–3029. https://doi.org/10.1039/C5EE02179K.

(21) Esch, F.; Fabris, S.; Zhou, L.; Montini, T.; Africh, C.; Fornasiero, P.; Comelli, G.; Rosei, R. Electron Localization Determines Defect Formation on Ceria Substrates. *Science* **2005**, *309* (5735), 752–755. https://doi.org/10.1126/science.1111568.

(22) Skorodumova, N. V.; Simak, S. I.; Lundqvist, B. I.; Abrikosov, I. A.; Johansson, B. Quantum Origin of the Oxygen Storage Capability of Ceria. *Phys. Rev. Lett.* **2002**, *89* (16), 166601. https://doi.org/10.1103/PhysRevLett.89.166601.

(23) Sayle, T. X. T.; Caddeo, F.; Zhang, X.; Sakthivel, T.; Das, S.; Seal, S.; Ptasinska, S.; Sayle, D. C. Structure-Activity Map of Ceria Nanoparticles, Nanocubes, and Mesoporous Architectures. *Chem. Mater.* **2016**, *28* (20), 7287–7295. https://doi.org/10.1021/acs.chemmater.6b02536.

(24) Pirmohamed, T.; Dowding, J. M.; Singh, S.; Wasserman, B.; Heckert, E.; Karakoti, A. S.; King, J. E. S.; Seal, S.; Self, W. T. Nanoceria Exhibit Redox State-Dependent Catalase Mimetic Activity. *Chem. Commun.* **2010**, *46* (16), 2736. https://doi.org/10.1039/b922024k.

(25) Baldim, V.; Bedioui, F.; Mignet, N.; Margaill, I.; Berret, J.-F. The Enzyme-like Catalytic Activity of Cerium Oxide Nanoparticles and Its Dependency on Ce^{3+} Surface Area Concentration. *Nanoscale* **2018**, *10* (15), 6971–6980. https://doi.org/10.1039/C8NR00325D.

(26) Bernal, S.; Calvino, J. J.; Cifredo, G. A.; Gatica, J. M.; Omil, J. A. P.; Pintado, J. M. Hydrogen Chemisorption on Ceria: Influence of the Oxide Surface Area and Degree of Reduction. *J. Chem. Soc. Faraday Trans.* **1993**, *89* (18), 3499–3505. https://doi.org/10.1039/FT9938903499.

(27) Bulfin, B.; Lowe, A. J.; Keogh, K. A.; Murphy, B. E.; Lübben, O.; Krasnikov, S. A.; Shvets, I. V. Analytical Model of CeO_2 Oxidation and Reduction. *J. Phys. Chem. C* **2013**, *117* (46), 24129–24137. https://doi.org/10.1021/jp406578z.

(28) Pettinger, N. W.; Empey, J. M.; Fröbel, S.; Kohler, B. Photoreductive Dissolution of Cerium Oxide Nanoparticles and Their Size-Dependent Absorption Properties. *Phys. Chem. Chem. Phys.* **2020**, *22* (10), 5756–5764. https://doi.org/10.1039/C9CP06579B.

(29) Werner, K.; Weng, X.; Calaza, F.; Sterrer, M.; Kropp, T.; Paier, J.; Sauer, J.; Wilde, M.; Fukutani, K.; Shaikhutdinov, S.; Freund, H.-J. Toward an Understanding of Selective Alkyne Hydrogenation on Ceria: On the Impact of O Vacancies on H_2 Interaction with CeO_2 (111). *J. Am. Chem. Soc.* **2017**, *139* (48), 17608–17616. https://doi.org/10.1021/jacs.7b10021.

(30) Vilé, G.; Bridier, B.; Wichert, J.; Pérez-Ramírez, J. Ceria in Hydrogenation Catalysis: High Selectivity in the Conversion of Alkynes to Olefins. *Angew. Chem. Int. Ed.* **2012**, *51* (34), 8620–8623. https://doi.org/10.1002/anie.201203675.

(31) García-Melchor, M.; Bellarosa, L.; López, N. Unique Reaction Path in Heterogeneous Catalysis: The Concerted Semi-Hydrogenation of Propyne to Propene on CeO_2. *ACS Catal.* **2014**, *4* (11), 4015–4020. https://doi.org/10.1021/cs5011508.

(32) Chang, K.; Zhang, H.; Cheng, M.; Lu, Q. Application of Ceria in CO_2 Conversion Catalysis. *ACS Catal.* **2020**, *10* (1), 613–631. https://doi.org/10.1021/acscatal.9b03935.

(33) Sohlberg, K.; Pantelides, S. T.; Pennycook, S. J. Interactions of Hydrogen with CeO_2. *J. Am. Chem. Soc.* **2001**, *123* (27), 6609–6611. https://doi.org/10.1021/ja004008k.

(34) Luo, M.; Wang, Z.; Li, Y. C.; Li, J.; Li, F.; Lum, Y.; Nam, D.-H.; Chen, B.; Wicks, J.; Xu, A.; Zhuang, T.; Leow, W. R.; Wang, X.; Dinh, C.-T.; Wang, Y.; Wang, Y.; Sinton, D.; Sargent, E. H. Hydroxide Promotes Carbon Dioxide Electroreduction to Ethanol on Copper via Tuning of Adsorbed Hydrogen. *Nat. Commun.* **2019**, *10* (1), 1–7. https://doi.org/10.1038/s41467-019-13833-8.

(35) Lu, M.; Zhang, Y.; Wang, Y.; Jiang, M.; Yao, X. Insight into Several Factors That Affect the Conversion between Antioxidant and Oxidant Activities of Nanoceria. *ACS Appl. Mater. Interfaces* **2016**, *8* (36), 23580–23590. https://doi.org/10.1021/acsami.6b08219.

(36) Nelson, B.; Johnson, M.; Walker, M.; Riley, K.; Sims, C. Antioxidant Cerium Oxide Nanoparticles in Biology and Medicine. *Antioxidants* **2016**, *5* (2), 15. https://doi.org/10.3390/antiox5020015.

(37) Andreescu, D.; Bulbul, G.; Özel, R. E.; Hayat, A.; Sardesai, N.; Andreescu, S. Applications and Implications of Nanoceria Reactivity: Measurement Tools and Environmental Impact. *Env. Sci Nano* **2014**, *1* (5), 445–458. https://doi.org/10.1039/C4EN00075G.

(38) Trovarelli, A.; Fornasiero, P. *Catalysis by Ceria and Related Materials*; Imperial College Press, 2013.

(39) Zhang, C.; Yu, Y.; Grass, M. E.; Dejoie, C.; Ding, W.; Gaskell, K.; Jabeen, N.; Hong, Y. P.; Shavorskiy, A.; Bluhm, H.; Li, W.-X.; Jackson, G. S.; Hussain, Z.; Liu, Z.; Eichhorn, B. W. Mechanistic Studies of Water Electrolysis and Hydrogen Electro-Oxidation on High Temperature Ceria-Based Solid Oxide Electrochemical Cells. *J. Am. Chem. Soc.* **2013**, *135* (31), 11572–11579. https://doi.org/10.1021/ja402604u.

(40) Bevan, D. J. M.; Kordis, J. Mixed Oxides of the Type MO_2 (Fluorite)—M_2O_3—I Oxygen Dissociation Pressures and Phase Relationships in the System CeO_2□Ce_2O_3 at High Temperatures. *J. Inorg. Nucl. Chem.* **1964**, *26* (9), 1509–1523. https://doi.org/10.1016/0022-1902(64)80038-5.

(41) Van de Walle, C. G.; Neugebauer, J. Universal Alignment of Hydrogen Levels in Semiconductors, Insulators and Solutions. *Nature* **2003**, *423* (6940), 626–628. https://doi.org/10.1038/nature01665.

(42) Norby, T.; Widerøe, M.; Glöckner, R.; Larring, Y. Hydrogen in Oxides. *Dalton Trans* **2004**, No. 19, 3012–3018. https://doi.org/10.1039/B403011G.

(43) Shahed, S. M. F.; Hasegawa, T.; Sainoo, Y.; Watanabe, Y.; Isomura, N.; Beniya, A.; Hirata, H.; Komeda, T. STM and XPS Study of CeO_2(111) Reduction by Atomic Hydrogen. *Surf. Sci.* **2014**, *628*, 30–35. https://doi.org/10.1016/j.susc.2014.05.008.

(44) Vicario, G.; Balducci, G.; Fabris, S.; de Gironcoli, S.; Baroni, S. Interaction of Hydrogen with Cerium Oxide Surfaces: A Quantum Mechanical Computational Study. *J. Phys. Chem. B* **2006**, *110* (39), 19380–19385. https://doi.org/10.1021/jp061375v.

(45) Paier, J.; Penschke, C.; Sauer, J. Oxygen Defects and Surface Chemistry of Ceria: Quantum Chemical Studies Compared to Experiment. *Chem. Rev.* **2013**, *113* (6), 3949–3985. https://doi.org/10.1021/cr3004949.

(46) Zhou, C.; Zhang, B.; Hu, P.; Wang, H. An Effective Structural Descriptor to Quantify the Reactivity of Lattice Oxygen in CeO_2 Subnano-Clusters. *Phys. Chem. Chem. Phys.* **2020**, 10.1039.C9CP05805B. https://doi.org/10.1039/C9CP05805B.

(47) Warren, J. J.; Tronic, T. A.; Mayer, J. M. Thermochemistry of Proton-Coupled Electron Transfer Reagents and Its Implications. *Chem. Rev.* **2010**, *110* (12), 6961–7001. https://doi.org/10.1021/cr100085k.

(48) Agarwal, R. G.; Wise, C. F.; Coste, S. C.; Groff, B. D.; Heuer, A. H.; Noh, H.; Parada, G. A.; Warren, J. J.; Mayer, J. M. Free Energies of Proton-Coupled Electron Transfer Reagents. *Prep.*

(49) Bezdek, M. J.; Pappas, I.; Chirik, P. J. Determining and Understanding N-H Bond Strengths in Synthetic Nitrogen Fixation Cycles. In *Nitrogen Fixation*; Nishibayashi, Y., Ed.; Topics in Organometallic Chemistry; Springer International Publishing: Cham, 2017; pp 1–21. https://doi.org/10.1007/3418_2016_8.

(50) Gentry, E. C.; Knowles, R. R. Synthetic Applications of Proton-Coupled Electron Transfer. *Acc. Chem. Res.* **2016**, *49* (8), 1546–1556. https://doi.org/10.1021/acs.accounts.6b00272.

(51) Chalkley, M. J.; Peters, J. C. Relating N-H Bond Strengths to the Overpotential for Catalytic Nitrogen Fixation: Relating N-H Bond Strengths to the Overpotential for Catalytic Nitrogen Fixation. *Eur. J. Inorg. Chem.* **2020**, *2020* (15–16), 1353–1357. https://doi.org/10.1002/ejic.202000232.

(52) Darcy, J. W.; Koronkiewicz, B.; Parada, G. A.; Mayer, J. M. A Continuum of Proton-Coupled Electron Transfer Reactivity. *Acc. Chem. Res.* **2018**, *51* (10), 2391–2399. https://doi.org/10.1021/acs.accounts.8b00319.

(53) Roth, J. P. Application of the Marcus Cross Relation to Hydrogen Atom Transfer Reactions. *Science* **2001**, *294* (5551), 2524–2526. https://doi.org/10.1126/science.1066130.

(54) Wise, C. F.; Mayer, J. M. Electrochemically Determined O–H Bond Dissociation Free Energies of NiO Electrodes Predict Proton-Coupled Electron Transfer Reactivity. *J. Am. Chem. Soc.* **2019**, *141* (38), 14971–14975. https://doi.org/10.1021/jacs.9b07923.

(55) Wise, C. F.; Agarwal, R. G.; Mayer, J. M. Determining Proton-Coupled Standard Potentials and X–H Bond Dissociation Free Energies in Nonaqueous Solvents Using Open-Circuit Potential Measurements. *J. Am. Chem. Soc.* **2020**, jacs.0c01032. https://doi.org/10.1021/jacs.0c01032.

(56) Coppel, Y.; Spataro, G.; Pagès, C.; Chaudret, B.; Maisonnat, A.; Kahn, M. L. Full Characterization of Colloidal Solutions of Long-Alkyl-Chain-Amine-Stabilized ZnO Nanoparticles by NMR Spectroscopy: Surface State, Equilibria, and Affinity. *Chem. - Eur. J.* **2012**, *18* (17), 5384–5393. https://doi.org/10.1002/chem.201102050.

(57) Shim, M.; Guyot-Sionnest, P. N-Type Colloidal Semiconductor Nanocrystals. *Nature* **2000**, *407* (6807), 981–983. https://doi.org/10.1038/35039577.

(58) Kölle, U.; Grützel, M. Organometallic Rhodium(III) Complexes as Catalysts for the Photoreduction of Protons to Hydrogen on Colloidal TiO_2. *Angew. Chem. Int. Ed. Engl.* **1987**, *26* (6), 567–570. https://doi.org/10.1002/anie.198705671.

(59) Wang, C.; Pagel, R.; Bahnemann, D. W.; Dohrmann, J. K. Quantum Yield of Formaldehyde Formation in the Presence of Colloidal TiO_2-Based Photocatalysts: Effect of Intermittent Illumination, Platinization, and Deoxygenation. *J. Phys. Chem. B* **2004**, *108* (37), 14082–14092. https://doi.org/10.1021/jp048046s.

(60) Buonsanti, R.; Llordes, A.; Aloni, S.; Helms, B. A.; Milliron, D. J. Tunable Infrared Absorption and Visible Transparency of Colloidal Aluminum-Doped Zinc Oxide Nanocrystals. *Nano Lett.* **2011**, *11* (11), 4706–4710. https://doi.org/10.1021/nl203030f.

(61) Cohn, A. W.; Kittilstved, K. R.; Gamelin, D. R. Tuning the Potentials of “Extra” Electrons in Colloidal *n*-Type ZnO Nanocrystals via Mg^{2+} Substitution. *J. Am. Chem. Soc.* **2012**, *134* (18), 7937–7943. https://doi.org/10.1021/ja3019934.

(62) Ribot, F.; Escax, V.; Roiland, C.; Sanchez, C.; Martins, J. C.; Biesemans, M.; Verbruggen, I.; Willem, R. *In Situ* Evaluation of Interfacial Affinity in CeO_2 Based Hybrid Nanoparticles by Pulsed Field Gradient NMR. *Chem. Commun.* **2005**, No. 8, 1019. https://doi.org/10.1039/b411629a.

(63) Schneider, J.; Matsuoka, M.; Takeuchi, M.; Zhang, J.; Horiuchi, Y.; Anpo, M.; Bahnemann, D. W. Understanding TiO_2 Photocatalysis: Mechanisms and Materials. *Chem. Rev.* **2014**, *114* (19), 9919–9986. https://doi.org/10.1021/cr5001892.

(64) Cohn, A. W.; Janßen, N.; Mayer, J. M.; Gamelin, D. R. Photocharging ZnO Nanocrystals: Picosecond Hole Capture, Electron Accumulation, and Auger Recombination. *J. Phys. Chem. C* **2012**, *116* (38), 20633–20642. https://doi.org/10.1021/jp3075942.

(65) Grauer, D. C.; Alivisatos, A. P. Ligand Dissociation Mediated Charge Transfer Observed at Colloidal $W_{18}O_{49}$ Nanoparticle Interfaces. *Langmuir* **2014**, *30* (9), 2325–2328. https://doi.org/10.1021/la404019v.

(66) Gambardella, A. A.; Bjorge, N. S.; Alspaugh, V. K.; Murray, R. W. Voltammetry of Diffusing 2 Nm Iridium Oxide Nanoparticles. *J. Phys. Chem. C* **2011**, *115* (44), 21659–21665. https://doi.org/10.1021/jp206987z.

(67) Brozek, C. K.; Hartstein, K. H.; Gamelin, D. R. Potentiometric Titrations for Measuring the Capacitance of Colloidal Photodoped ZnO Nanocrystals. *J. Am. Chem. Soc.* **2016**, *138* (33), 10605–10610. https://doi.org/10.1021/jacs.6b05848.

(68) Damatov, D.; Laga, S. M.; Mader, E. A.; Peng, J.; Agarwal, R. G.; Mayer, J. M. Redox Reactivity of Colloidal Nanoceria and Use of Optical Spectra as an In Situ Monitor of Ce Oxidation States. *Inorg. Chem.* **2018**, *57* (22), 14401–14408. https://doi.org/10.1021/acs.inorgchem.8b02598.

(69) Nachimuthu, P.; Shih, W.-C.; Liu, R.-S.; Jang, L.-Y.; Chen, J.-M. The Study of Nanocrystalline Cerium Oxide by X-Ray Absorption Spectroscopy. *J. Solid State Chem.* **2000**, *149* (2), 408–413. https://doi.org/10.1006/jssc.1999.8566.

(70) Cafun, J.-D.; Kvashnina, K. O.; Casals, E.; Puntes, V. F.; Glatzel, P. Absence of Ce^{3+} Sites in Chemically Active Colloidal Ceria Nanoparticles. *ACS Nano* **2013**, *7* (12), 10726–10732. https://doi.org/10.1021/nn403542p.

(71) Zhang, J.; Wu, Z.; Liu, T.; Hu, T.; Wu, Z.; Ju, X. XANES Study on the Valence Transitions in Cerium Oxide Nanoparticles. *J. Synchrotron Radiat.* **2001**, *8*, 531. https://doi.org/10.1107/S0909049500016022.

(72) Wang, Z. L.; Feng, X. Polyhedral Shapes of CeO_2 Nanoparticles. *J. Phys. Chem. B* **2003**, *107* (49), 13563–13566. https://doi.org/10.1021/jp036815m.

(73) Perrichon, V.; Laachir, A.; Bergeret, G.; Fréty, R.; Tournayan, L.; Touret, O. Reduction of Cerias with Different Textures by Hydrogen and Their Reoxidation by Oxygen. *J. Chem. Soc. Faraday Trans.* **1994**, *90* (5), 773–781. https://doi.org/10.1039/FT9949000773.

(74) Wu, Z.; Cheng, Y.; Tao, F.; Daemen, L.; Foo, G. S.; Nguyen, L.; Zhang, X.; Beste, A.; Ramirez-Cuesta, A. J. Direct Neutron Spectroscopy Observation of Cerium Hydride Species on a Cerium Oxide Catalyst. *J. Am. Chem. Soc.* **2017**, *139* (28), 9721–9727. https://doi.org/10.1021/jacs.7b05492.

(75) Li, Z.; Werner, K.; Qian, K.; You, R.; Płucienik, A.; Jia, A.; Wu, L.; Zhang, L.; Pan, H.; Kuhlenbeck, H.; Shaikhutdinov, S.; Huang, W.; Freund, H.-J. Oxidation of Reduced Ceria by Incorporation of Hydrogen. *Angew. Chem. Int. Ed.* **2019**, *58*, 2–10. https://doi.org/10.1002/anie.201907117.

(76) Ji, P.; Sawano, T.; Lin, Z.; Urban, A.; Boures, D.; Lin, W. Cerium-Hydride Secondary Building Units in a Porous Metal–Organic Framework for Catalytic Hydroboration and Hydrophosphination. *J. Am. Chem. Soc.* **2016**, *138* (45), 14860–14863. https://doi.org/10.1021/jacs.6b10055.

(77) Moon, J.; Cheng, Y.; Daemen, L. L.; Li, M.; Polo-Garzon, F.; Ramirez-Cuesta, A. J.; Wu, Z. Discriminating the Role of Surface Hydride and Hydroxyl for Acetylene Semihydrogenation over Ceria through *In Situ* Neutron and Infrared Spectroscopy. *ACS Catal.* **2020**, 5278–5287. https://doi.org/10.1021/acscatal.0c00808.

(78) García-Melchor, M.; López, N. Homolytic Products from Heterolytic Paths in H_2 Dissociation on Metal Oxides: The Example of CeO_2. *J. Phys. Chem. C* **2014**, *118* (20), 10921–10926. https://doi.org/10.1021/jp502309r.

(79) Copéret, C.; Estes, D. P.; Larmier, K.; Searles, K. Isolated Surface Hydrides: Formation, Structure, and Reactivity. *Chem. Rev.* **2016**, *116* (15), 8463–8505. https://doi.org/10.1021/acs.chemrev.6b00082.

(80) Gill, L.; Beste, A.; Chen, B.; Li, M.; Mann, A. K. P.; Overbury, S. H.; Hagaman, E. W. Fast MAS ^1H NMR Study of Water Adsorption and Dissociation on the (100) Surface of Ceria Nanocubes: A Fully Hydroxylated, Hydrophobic Ceria Surface. *J. Phys. Chem. C* **2017**, *121* (13), 7450–7465. https://doi.org/10.1021/acs.jpcc.6b12375.

(81) Chen, J.; Hope, M. A.; Lin, Z.; Wang, M.; Liu, T.; Halat, D. M.; Wen, Y.; Chen, T.; Ke, X.; Magusin, P. C. M. M.; Ding, W.; Xia, X.; Wu, X.-P.; Gong, X.-Q.; Grey, C. P.; Peng, L. Interactions of Oxide Surfaces with Water Revealed with Solid-State NMR Spectroscopy. *J. Am. Chem. Soc.* **2020**, jacs.0c03760. https://doi.org/10.1021/jacs.0c03760.

(82) Chen, B.; Ma, Y.; Ding, L.; Xu, L.; Wu, Z.; Yuan, Q.; Huang, W. Reactivity of Hydroxyls and Water on a CeO_2 (111) Thin Film Surface: The Role of Oxygen Vacancy. *J. Phys. Chem. C* **2013**, *117* (11), 5800–5810. https://doi.org/10.1021/jp312406f.

(83) Goris, B.; Turner, S.; Bals, S.; Van Tendeloo, G. Three-Dimensional Valency Mapping in Ceria Nanocrystals. *ACS Nano* **2014**, *8* (10), 10878–10884. https://doi.org/10.1021/nn5047053.

(84) Spadaro, M. C.; Luches, P.; Bertoni, G.; Grillo, V.; Turner, S.; Van Tendeloo, G.; Valeri, S.; D'Addato, S. Influence of Defect Distribution on the Reducibility of CeO_{2-x} Nanoparticles. *Nanotechnology* **2016**, *27* (42), 425705. https://doi.org/10.1088/0957-4484/27/42/425705.

(85) Liu, H.; Brozek, C. K.; Sun, S.; Lingerfelt, D. B.; Gamelin, D. R.; Li, X. A Hybrid Quantum-Classical Model of Electrostatics in Multiply Charged Quantum Dots. *J. Phys. Chem. C* **2017**, *121* (46), 26086–26095. https://doi.org/10.1021/acs.jpcc.7b08224.

(86) Gómez, R.; Orts, J. M.; Álvarez-Ruiz, B.; Feliu, J. M. Effect of Temperature on Hydrogen Adsorption on Pt(111), Pt(110), and Pt(100) Electrodes in 0.1 M $HClO_4$. *J. Phys. Chem. B* **2004**, *108* (1), 228–238. https://doi.org/10.1021/jp034982g.

(87) Mitchell, K. J.; Abboud, K. A.; Christou, G. Atomically-Precise Colloidal Nanoparticles of Cerium Dioxide. *Nat. Commun.* **2017**, *8* (1), 1445. https://doi.org/10.1038/s41467-017-01672-4.

(88) Buchanan, C. A.; Ko, E.; Cira, S.; Balasubramanian, M.; Goldsmith, B. R.; Singh, N. Structures and Free Energies of Cerium Ions in Acidic Electrolytes. *Inorg. Chem.* **2020**, *59* (17), 12552–12563. https://doi.org/10.1021/acs.inorgchem.0c01645.

(89) Duchoň, T.; Aulická, M.; Schwier, E. F.; Iwasawa, H.; Zhao, C.; Xu, Y.; Veltruská, K.; Shimada, K.; Matolín, V. Covalent versus Localized Nature of 4f Electrons in Ceria: Resonant Angle-Resolved Photoemission Spectroscopy and Density Functional Theory. *Phys. Rev. B* **2017**, *95* (16), 165124. https://doi.org/10.1103/PhysRevB.95.165124.

(90) Prieur, D.; Bonani, W.; Popa, K.; Walter, O.; Kriegsman, K. W.; Engelhard, M. H.; Guo, X.; Eloirdi, R.; Gouder, T.; Beck, A.; Vitova, T.; Scheinost, A. C.; Kvashnina, K.; Martin, P. Size Dependence of Lattice Parameter and Electronic Structure in CeO_2 Nanoparticles. *Inorg. Chem.* **2020**, *59* (8), 5760–5767. https://doi.org/10.1021/acs.inorgchem.0c00506.

(91) Jeong, H.; Shin, D.; Kim, B.; Bae, J.; Shin, S.; Choe, C.; Han, J. W.; Lee, H. Controlling the Oxidation State of Pt Single Atoms for Maximizing Catalytic Activity. *Angew. Chem. Int. Ed.* **2020**, anie.202009776. https://doi.org/10.1002/anie.202009776.

(92) Dejoie, C.; Yu, Y.; Bernardi, F.; Tamura, N.; Kunz, M.; Marcus, M. A.; Huang, Y.-L.; Zhang, C.; Eichhorn, B. W.; Liu, Z. Potential Control of Oxygen Non-Stoichiometry in Cerium Oxide and Phase Transition Away from Equilibrium. *ACS Appl. Mater. Interfaces* **2020**, *12* (28), 31514–31521. https://doi.org/10.1021/acsami.0c08284.

(93) Hillert, M.; Jansson, B. Thermodynamic Model for Nonstoichiometric Ionic Phases - Application to CeO_{2-x}. *J. Am. Ceram. Soc.* **1986**, *69* (10), 732–734. https://doi.org/10.1111/j.1151-2916.1986.tb07334.x.

(94) Chueh, W. C.; Falter, C.; Abbott, M.; Scipio, D.; Furler, P.; Haile, S. M.; Steinfeld, A. High-Flux Solar-Driven Thermochemical Dissociation of CO_2 and H_2O Using Nonstoichiometric Ceria. *Science* **2010**, *330* (6012), 1797–1801. https://doi.org/10.1126/science.1197834.

(95) Abanades, S.; Legal, A.; Cordier, A.; Peraudeau, G.; Flamant, G.; Julbe, A. Investigation of Reactive Cerium-Based Oxides for H_2 Production by Thermochemical Two-Step Water-Splitting. *J. Mater. Sci.* **2010**, *45* (15), 4163–4173. https://doi.org/10.1007/s10853-010-4506-4.

(96) Rao, C. N. R.; Dey, S. Solar Thermochemical Splitting of Water to Generate Hydrogen. *Proc. Natl. Acad. Sci.* **2017**, *114* (51), 13385–13393. https://doi.org/10.1073/pnas.1700104114.

(97) Crandall, R. S.; Wojtowicz, P. J.; Faughnan, B. W. Theory and Measurement of the Change in Chemical Potential of Hydrogen in Amorphous H_xWO_3 as a Function of the Stoichiometric Parameter x. *Solid State Commun.* **1976**, *18* (11), 1409–1411. https://doi.org/10.1016/0038-1098(76)90357-4.

(98) Delley, M. F.; Wu, Z.; Mundy, M. E.; Ung, D.; Cossairt, B. M.; Wang, H.; Mayer, J. M. Hydrogen on Cobalt Phosphide. *J. Am. Chem. Soc.* **2019**, *141* (38), 15390–15402. https://doi.org/10.1021/jacs.9b07986.

(99) Zakaryan, H. A.; Kvashnin, A. G.; Oganov, A. R. Stable Reconstruction of the (110) Surface and Its Role in Pseudocapacitance of Rutile-like RuO_2. *Sci. Rep.* **2017**, *7* (1), 10357. https://doi.org/10.1038/s41598-017-10331-z.

Table of Contents Graphic: